



HAL
open science

On the role of impurities on spheroidal graphite degeneracy in cast irons

Bernadette Domengès, Mayerling Martinez Celis, Florent Moisy, Jacques Lacaze, Babette Tonn

► **To cite this version:**

Bernadette Domengès, Mayerling Martinez Celis, Florent Moisy, Jacques Lacaze, Babette Tonn. On the role of impurities on spheroidal graphite degeneracy in cast irons. *Carbon*, 2021, 172, pp.529-541. 10.1016/j.carbon.2020.10.030 . hal-03182250v1

HAL Id: hal-03182250

<https://hal.science/hal-03182250v1>

Submitted on 24 Oct 2020 (v1), last revised 26 Mar 2021 (v2)

HAL is a multi-disciplinary open access archive for the deposit and dissemination of scientific research documents, whether they are published or not. The documents may come from teaching and research institutions in France or abroad, or from public or private research centers.

L'archive ouverte pluridisciplinaire **HAL**, est destinée au dépôt et à la diffusion de documents scientifiques de niveau recherche, publiés ou non, émanant des établissements d'enseignement et de recherche français ou étrangers, des laboratoires publics ou privés.

On the role of impurities on spheroidal graphite degeneracy in cast irons

Bernadette Domengès^{1*}, Mayerling Martinez Celis¹, Florent Moisy¹, Jacques Lacaze^{2*},
Babette Tonn³

¹ *Laboratoire de Cristallographie et Science des Matériaux, Normandie Univ, ENSICAEN, UNICAEN, CNRS, CRISMAT, 6 Boulevard du Maréchal Juin, 14050 Caen Cedex 4, France*

² *CIRIMAT, Université de Toulouse, ENSIACET, 4 allée Emile Monso – BP44362, 31030 Toulouse Cedex 4, France,*

³ *Clausthal University of Technology – Institute of Metallurgy, Robert-Koch-Straße 42, 38678 Clausthal-Zellerfeld, Germany*

Abstract

Though manufacturing spheroidal graphite cast irons is a well-established industrial process, good nodularity which is essential for mechanical properties may be hampered by several factors. Amongst them is the presence of impurities at trace level which lead to the growth of protrusions and the question is how they can destroy the spheroidizing effect of magnesium. For the first time, it is shown that such impurities are present together with magnesium at the interface between spheroid and protrusion. For getting this result, site-specific electron transparent lamellae were prepared using Focused Ion Beam and characterized at nanometric scale using atomic resolution scanning-transmission electron microscope. It is also shown by automatic crystal orientation mapping that there is no definite crystallographic relationship between protrusions and underlying spheroids.

Keywords: focused ion-electron dual beam, scanning transmission electron microscopy, spheroidal graphite, degenerate graphite, cast iron

1. Introduction

Degeneracy of spheroidal graphite in cast irons is contemporary to the discovery that small additions of cerium [1] or magnesium [2] to the melt before casting changes the graphite shape from lamellar to spheroidal. The nodularity of spheroidal graphite is known to be sensitive to casting size, i.e. to cooling rate. When casting heavy-section components, this leads to the practice of increasing the amount of spheroidizing elements (Mg and Ce). In such a case, there is a risk of so-called over-treatment with the appearance of exploded spheroids

* Corresponding authors. E-mail: bernadette.domenges@ensicaen.fr (Bernadette Domengès)
jacques.lacaze@toulouse-inp.fr (Jacques Lacaze)

[3] and of chunky graphite (see for example the reviews by Lacaze *et al.* [4] and Baer [5]). If instead fading of the spheroidizing treatment occurs, spheroids may degenerate by the growth of coarse lamellar protrusions developing at the outer surface of the spheroids and giving rise to so-called compact graphite.

Moreover, the possible negative effect of low-level impurities on graphite nodularity was already mentioned in the patent granted to Millis *et al.* [2]. Since then, extensive experimental work has been carried out to quantify this effect in an attempt to control it. This led Thielemann suggesting a quality factor depending on the content of the melt charge in the most known impurities at that time, namely Al, As, Bi, Pb, Sb, Sn and Ti [6]. Reynaud provided more recently a review on the effect and critical level of all trace elements that are known to affect graphite shape in cast irons [7]. Though other quality indexes have been suggested in this review, the one proposed by Thielemann remains the most precise and comprehensive even though not giving any information on the way trace elements may interfere with the spheroidizing elements, in particular not accounting for Mg and Ce contents.

A wealth of works has been done to clarify the mechanism of spheroidal growth and the role of both spheroidizers and impurities. While several models for spheroidal growth have been proposed, none has yet been fully accepted (see for example the literature review in Stefanescu *et al.* [8] and Lacaze *et al.* [9]) which may explain why there is no consensus on the way trace elements affect graphite growth. However, graphite in cast irons does contain a significant quantity of foreign elements as proved by chemical analysis of extracted graphite particles [10 - 12] as well as by secondary ion mass spectroscopy (SIMS) [13 - 18]. Accordingly, there is no doubt that foreign elements do adsorb at the surface of growing graphite particles, and that part of them get then absorbed within graphite during solidification and cooling to room temperature. The possibility of adsorption of several elements on graphite has recently been quantified by first principle calculations [19].

However, very few of the attempts carried out to evidence enrichment in trace elements at the surface of graphite particles have been successful. Verhoeven and co-workers could detect oxygen and sulfur [20] and tellurium [21] by Auger analysis which is sensitive to the outermost atom layers but has a detection limit of several per cents. Also using Auger, Liu *et al.* [22] and Dekker *et al.* [23] detected Sb at the interface between graphite and matrix when this element was added to spheroidal graphite cast irons to counteract the tendency of Ce to promote exploded and chunky graphite. Energy Dispersive X-Ray spectrometry (EDS) and Electron Probe Micro-Analyzer (EPMA) techniques have also been extensively used, the

latter detecting significantly lower concentrations. Using an EPMA equipped with a field electron gun (FEG), Bourdie et al. [18] could decrease the detection limit for Al and Mg to a few tens of ppm when a low accelerating voltage was used together with long enough counting times. Provided care was taken in the set-up of the analysis conditions, foreign elements could thus be detected with some success in bulk graphite of cast irons [18, 24 – 26]. However, EPMA has a spatial resolution of a couple of microns which makes it less useful for precisely locating trace elements. Quite recently, an investigation at atomic scale has been attempted by Qing et al. [27] using atom probe when they encountered the same problem as with SIMS, namely mass interferences which suppress the possibility of detecting elements such as magnesium.

Hence, it appears that high-resolution scanning-transmission electron microscopy associated with EDS analysis technique is the most powerful tool at the present time to look for the presence of foreign elements within graphite in cast irons. This work was thus intended at studying the transition between spheroids and graphite protrusions triggered by addition of trace element to a melt prepared for casting spheroidal cast iron. Following previous observations, a spheroidal cast iron doped with Pb was selected [28]. Much effort was then carried out to study the observed graphite degeneracies at the scale achievable with advanced electron microscopies. Both chemical and crystallographic information could be gained from this investigation.

2. Experimental procedure

2.1. Sample synthesis

A sample was machined from a block cast with a cast iron having the composition listed in Table 1. The melt had been prepared following a standard procedure to get spheroidal graphite, but it was also alloyed with Pb that led to graphite degeneracy [28]. Note that the final total content of Mg is at the upper limit of the usual range [7].

Table 1 – Sample composition*, balance Fe.

	C	Si	Mn	P	S	Mg	Pb	Ce	Sn
wt%	3.37	2.76	0.06	0.029	0.012	0.061	0.012	0.006	0.010
at%	13.61	4.77	0.053	0.045	0.018	0.122	0.003	0.002	0.004

* determined by combustion analysis for carbon and sulfur contents and by Optical Emission Spectroscopy with Inductively Coupled Plasma for the other elements

2.2. Methodology

The sample was ground down and polished using standard metallographic procedure. Figure 1(a) illustrates the kind of features that were looked for, namely a diametrical section of a graphite spheroid with outgrowths which here appear at both its right and upper left surface. The metallographic observations were made under polarized light which gives a contrast in the spheroid varying with the local orientation of the graphite layers. Four sectors emanating from the center of the spheroid are thus highlighted since the c axis of the graphite is approximately parallel to the radius of the spheroid at all points. In addition, the variations in contrast within each sector indicate the presence of sub-sectors that certainly facilitate the rotation of the stack. It should also be noted that the base of the upper left protrusion shows a graphite stack whose orientation differs from that of the sector from which it emanates, see the variation in contrast at the location indicated by the open arrow in Figure 1(a).

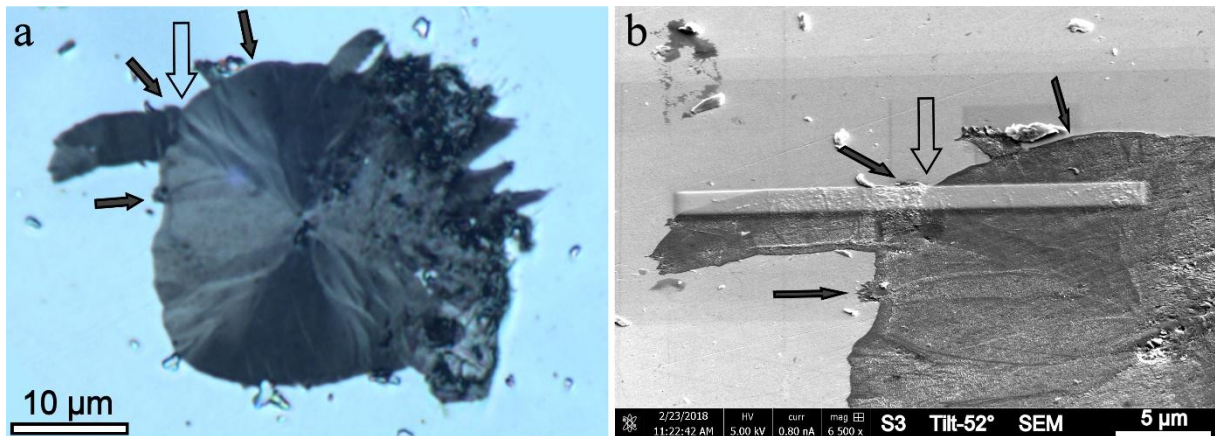


Fig. 1 (a) Optical micrograph under polarized light of a near-diametrical section of a graphite spheroid with outgrowths; (b) SEM image (tilted view) of the same sample (S3 stays for the third studied spheroid) after deposition of Pt-based mixture to protect the area to be milled. The open arrow locates the base of the protrusion and the black arrows show examples of contrast change. They have all been similarly located on both images.

Once a spheroid had been selected, the sample was introduced in the DualBeam (DB) system (FEI-HELIOS 600, Elstar Field Emission Scanning Electron Microscope column and Tomahawk Focused Ga Ion Beam column) equipped with Easy-lift manipulator designed for In-Situ Lift-Out thin lamella preparations [29, 30] and OXFORD Instruments Advanced X-Max 80 Silicon Drift Detector for EDS analyses. Indeed, the DB system allows both Scanning Electron Microscopy characterization and preparation of site-specific Transmission Electron Microscopy lamella using Ga^+ Focused Ion Beam. Following is the description of the analyses flow: i) SEM study (imaging and EDS analyses) of the top surface of the chosen spheroid; ii) preparation of the TEM lamella at a site including the spheroid and the outgrowth, see the protective Pt bar in figure 1(b); iii) during TEM lamella preparation,

successive SEM observations can be made on the cross-section on each side of the lamella as illustrated with the images in figure 2. Once the lamella is thin enough, it can in a first step be characterized in the DB which is equipped with a scanning transmission electron microscopy detector exhibiting several concentric sectors. They allow to produce simultaneously bright-field STEM images (DB-STEM-BF) and high angle annular dark field STEM images (DB-STEM-HAADF). Finally, the thin foil may be transferred to an atomic resolution scanning transmission electron microscope (JEM-ARM200F) which operates at 200 kV and is equipped with a cold FEG and with double TEM-STEM spherical aberration correctors. The latter ensure lattice TEM or STEM image resolution better than 0.1 nm and an electron nano-beam diameter below 0.15 nm at the entrance surface of the lamella for further analyses with JEOL EDS system. We chose not to include in the EDS results the Co, Ni and Cu elements as their presence is due to fluorescence phenomena in the TEM. Furthermore, their total content is most often lower than a few at%.

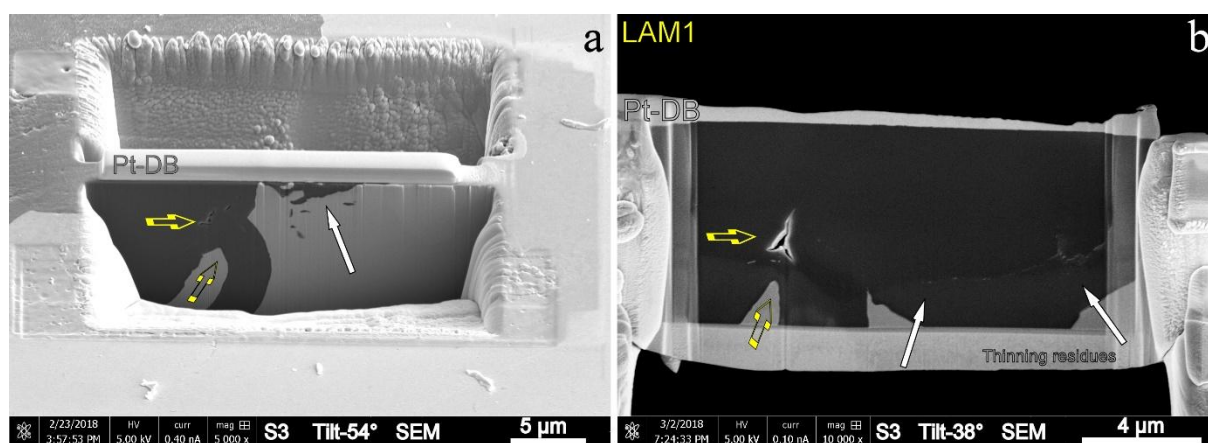


Fig. 2 SEM images (tilted views) of one side of the thin foil observed during the preparation of a lamella out from the spheroid S3. (a) After rough milling with the Ga^+ ion beam (lamella thickness is about 2 μm) and just before being cut and lifted out. (b) after lifting-out and further thinning. The white arrows point to the protrusion which is hardly observable in (a) while it has become prominent in (b).

In the DB, EDS measurements have been carried out on the top surface of the samples (not tilted) at 20 kV and by point counting during 10s live time. Raw EDS spectra were processed following standard procedures implemented in the dedicated software AZTEC (OXFORD Instruments). First, the back-ground noise was subtracted, and the detected peaks were refined by least squares method accounting for the expected ratio of K and L lines for light elements, L and M lines for heavy elements. This gave the so-called true-lines spectra which were scrutinized to look for all present elements. In addition to C, Fe and Si that were always present, Mg and O were most often present while Ca, S, Mn, Cl, P and Al were sometimes detected, but at very low content below 0.15 at % (0.25 wt%) for the first four and below 0.25 at% (0.55wt%) for P and Al. Further, Ag and Sn were systematically added to the

list of possible elements because they were detected in TEM-EDS measurements (see below) and must have been present at low level in the metallic charge used to prepare the cast iron. Pb has been detected as well during TEM-EDS measurements while Ce has never been detected.

For further processing of the data of each EDS spectrum, only elements for which the quantitative result (at% or wt%) was higher than 2σ were considered, with σ being the theoretical standard deviation for the counting conditions that were employed. For quantification, the EDS data were then processed using the ZAF (Z: atom weight; A: absorption; F: fluorescence) correction method and making use of the OXFORD library of standards recorded at 20 kV. Such a high electron beam energy is a compromise, enabling that at least one series of X-rays from every element will be excited, but leading to an increase in absorption correction and thus a loss of accuracy in quantification of light elements. The values obtained were finally normalized to 100%. For measurements within graphite, the C-K EDS signal is very strong compared to that of the other elements. First, because of the use of the 20kV accelerating voltage, the C ratio might be misestimated if not overestimated because of carbon contamination during the 10s duration of spectrum acquisition on each point. Second, the C ratio is mostly above 90 atomic % and this makes the quantification of the other elements rather inaccurate. Indeed, if we consider a relative error on the atomic quantification of about 2%, which is a typical value for our analyses without standardization, the remaining content of the sum of the other elements ranges from 8 to 12%. Summing up, EDS measurements are expected to give semi-quantitative information, meaning they allow quantitative trends to be observed though not giving accurate absolute values.

To determine the orientation relationship between a nodule and its outgrowths, Automatic Crystal Orientation Maps (ACOM) could be recorded on TEM lamellae. This was carried out in a FEI Tecnai transmission electron microscope operating at 300 kV and equipped with the ASTAR system [31]. Scanning of the electron beam over the selected area of the lamella was performed using a step size of 20 nm and a spot size of 8 nm. In each grid point, the electron nano-diffraction pattern is collected using an external CCD camera. The system then compares this experimental nano-diffraction pattern to pre-calculated patterns and selects the best-matching ones [32]. For the sake of simplicity, the comparison between experimental patterns and those created by the software was done using only one phase, the hexagonal form of graphite. When needed, Fe matrix was also introduced as a secondary phase. Compared to Electron Back Scattered Diffraction (EBSD) technique, ACOM has a much better spatial resolution (nanoscale) and reaches a better indexation rate on graphite

whose surface preparation for EBSD is very difficult. Crystal orientation maps and Inverse Pole Figures (IPF) given below always refer to z direction that is parallel to the axis of electron microscope column and perpendicular to the lamella plane.

3. Results

During the present study, seven spheroids with outgrowths were characterized from top surface or cross-section views with SEM imaging and EDS analyses. Among them, two thin foils have been prepared to be investigated with the ARM and only one with ASTAR. All observations showed that these outgrowths exhibit a plate-like morphology.

3.1. SEM and EDS on metallographic section

The base of the selected outgrowth in figure 1 was observed at higher magnification (Fig. 3). There are clear contrast changes on the surface which appears smooth in the right part of the underlying spheroid sector and rough in the outgrowth. Such topographic features are probably related to differences of resistance to grinding of graphite depending on its crystallographic orientation with respect to the metallographic surface. This agrees with the observation of the radial features evidenced in the optical image under polarized light (Fig. 1 (a)), which are related to orientation changes. It is also seen that areas with different orientations are intermixed between each other which must be associated with growth competition between the corresponding graphite stacking. This raises the question of whether sub-grains within the underlying sector played a role in the formation of the protrusion.

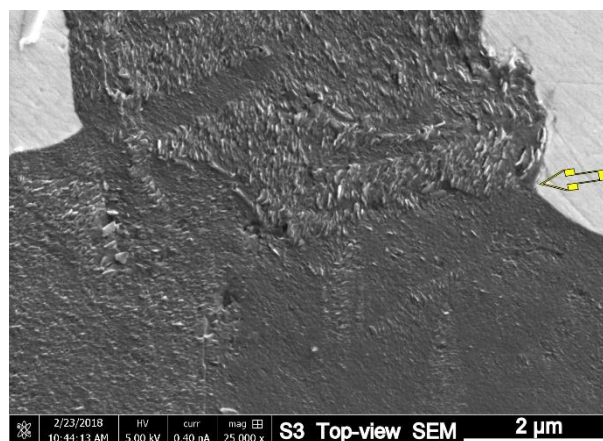


Fig. 3 SEM micrograph (top view) of the outgrowth on the graphite spheroid S3. Notice the change of surface aspect (open arrow) which relates to the change in crystallographic orientation evidenced in Fig. 1 (a).

Similar changes in surface aspect were observed for all degenerated graphite spheroids. The graphite precipitate in figure 4 appears much more degenerated than the previous one. From the surface aspect, change in orientation of the graphite stacking is associated with the

protrusion. The base of the protrusion may thus be imaged with the dotted line in between the two open arrows in figure 4(b).

EDS profiles were recorded along two perpendicular lines within the outgrowth, one longitudinal (Long-line) and the other transverse (Trans-line). Small dark grey spots can be seen along these lines, e.g. the one circled in figure 4(b). They correspond to the exact position of the electron beam during the acquisition of EDS spectra where carbon contamination accumulated. Measurements along these two lines gave similar results, and only the results along the transverse line are shown in figure 4(c) with the origin of the distance axis set at the middle point of the graphite outgrowth. The shaded areas on both sides relate to locations where the volume affected by the beam comprised both graphite and matrix, leading to higher and higher Fe and Si levels and to lower and lower carbon contents as the distance to the center of the protrusion increases. Mg was detected at significant levels, with a maximum value of 0.3at% (~0.5wt%), within the protrusion, and so was also P ($\leq 0.1\text{at}\%$, $\leq 0.25\text{wt}\%$) which is not shown for clarity of the graph. Oxygen was detected also, though appearing quite erratically. Mn was detected once with a content of 0.1 at% (0.45 wt%), while S, Ce, Sn and Pb were never detected.

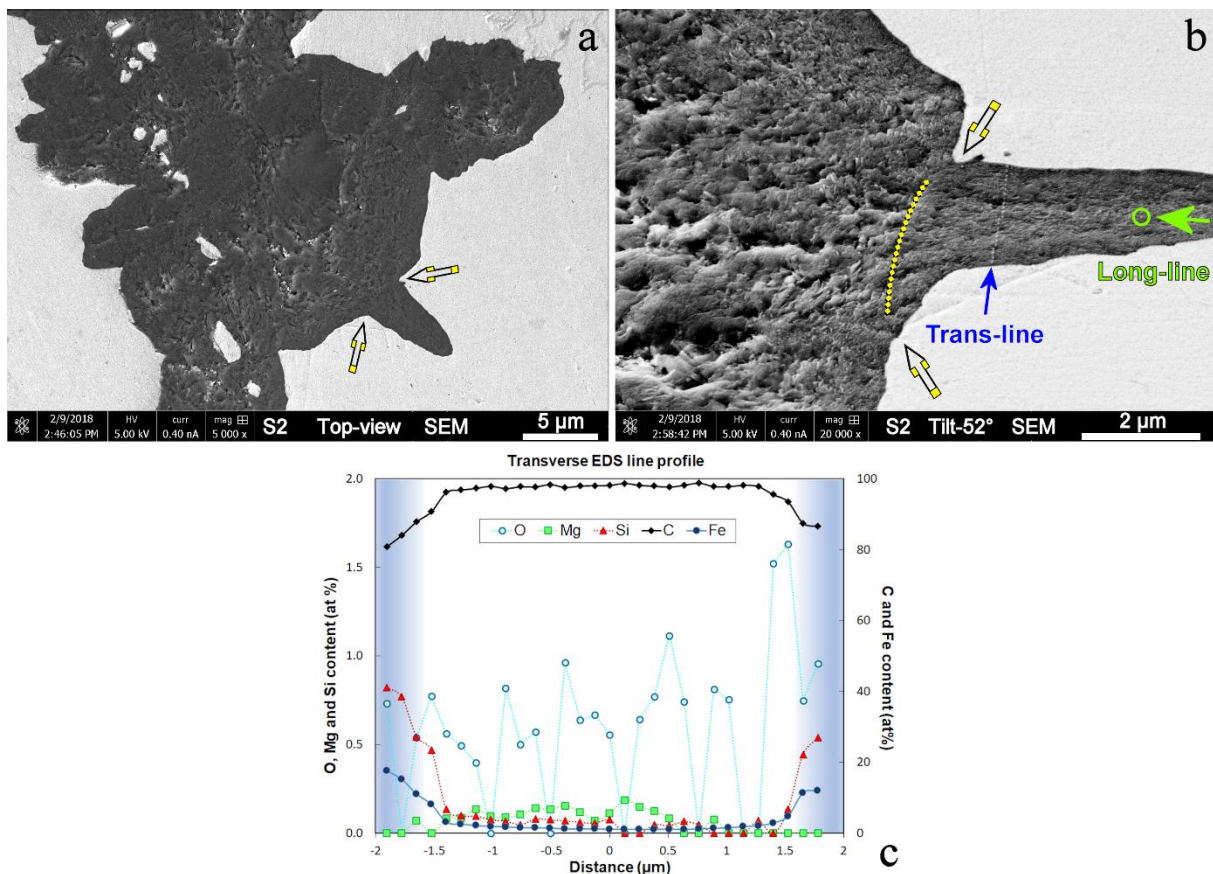


Fig. 4 (a) SEM micrograph (top view) of a degenerate graphite spheroid (S2) with outgrowths. Open arrows indicate the change point of surface features; (b) Higher magnification tilted view (52°) of the region of interest; (c) EDS line profiles, registered along transverse (Trans-line) direction of the outgrowth (see corresponding wt% line profile in Suppl-fig 1).

Figure 5 shows one outgrowth from another spheroid (S7) which appeared of interest owing to its length. However, a pollution area (red arrow) was observed and has been made more evident by enhancing the image contrast in Fig. 5-a. A transverse (Trans-line) line profile shown in Fig. 3 in the Supplementary File evidenced traces of Na, Cl, K and Ca associated to high levels of O in this pollution area. Fortunately, no contamination was present in the graphite and on the matrix on the other side of the protuberance. An EDS line profile was also recorded along the longitudinal (Long-line) direction which is plotted in Fig. 5-b. The same elements as before have been detected, i.e. C, Fe, O, Si, P and Mg, while Ce and Pb were not detected. Along the longitudinal line, S and Sn were each detected once in the protrusion, close to the interface with graphite spheroid and with a content below 0.04 at.% (0.1 S-wt% and 0.2 Sn-wt%). Along this line, the amount of carbon was most often higher than 90 at.% (80 wt%) except for the first four points at the start of the line-scan which were located in the matrix at the left of the protrusion, see the shaded area in Fig. 5b. It is seen that the silicon and iron contents decrease from the matrix to the protrusion as expected. On the other side of the protrusion, the amount of Fe decreases further at the end of the line profile when it reaches the bulk of the spheroid suggesting that the Fe level in the protrusion is mainly due to the contribution from the surrounding matrix.

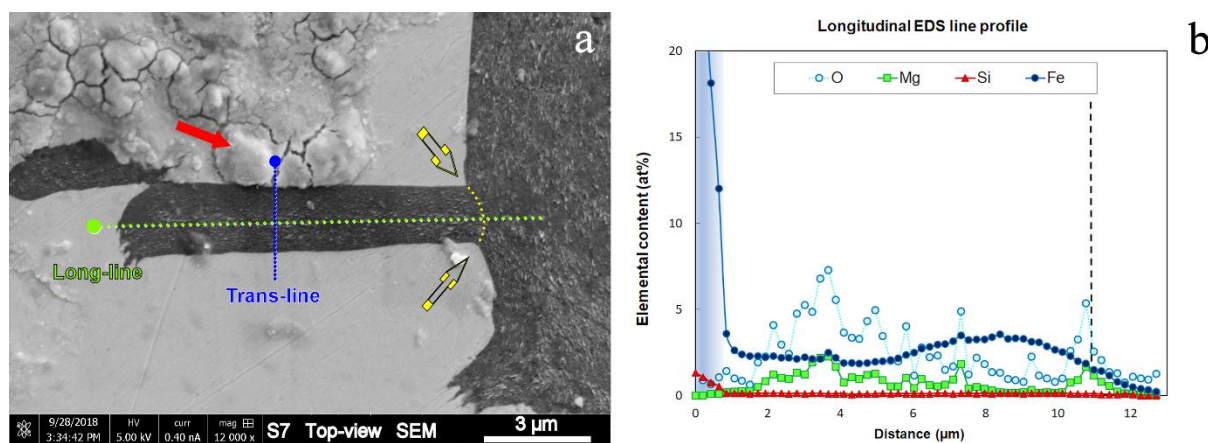


Fig. 5. (a) SEM micrograph (top view) of the outgrowth of another graphite precipitate (S7). Open arrows indicate changes in orientation of surface features with the dotted yellow curved line being the expected boundary between the spheroid and the outgrowth. The horizontal and vertical dotted lines show the location of the EDS lines, with the larger circles indicating the first measurement points; (b) EDS longitudinal line profile, with the shaded area corresponding to the matrix and the vertical dashed line to the limit between the protrusion and the spheroid (see corresponding wt% line profile in Suppl-fig 2); note pollution at the surface of the sample is observed (red arrow).

As in the previous case, Mg appears present at higher level for the measurement points located in graphite than in the surrounding matrix. It is worth noting that the contents in O and Mg appear to be somehow correlated with three common local maximums within the

protrusion. The decrease in the Fe, Mg and O contents at the right side of the profiles in figure 5 (b) strongly suggest that the elements detected in graphite are in fact present at the interface between graphite and matrix.

3.2. STEM in the Dual Beam system

Thin TEM lamellae were prepared in the median plane of the outgrowths shown in figure 3 and figure 5 and observed using the scanning transmission electron microscopy (STEM) detector of the DB system. This detector collects the electrons that pass through the sample so that the image contrast depends on the amount of signal absorbed and scattered by the sample. In the STEM-Bright Field (BF) imaging mode, where only transmitted electrons are collected, the contrast is mainly dependent on absorption: the thinner the lamella is and the lighter (Z atomic number) the present elements are, the brighter is the image. BF mode reveals grain boundaries as well. In the STEM-High Angle Annular Dark Field (HAADF) mode, where highly scattered electrons are collected, the contrast depends mainly on Z atomic number, the heavier the brighter. These two imaging modes provide complementary images (

Fig. 6).

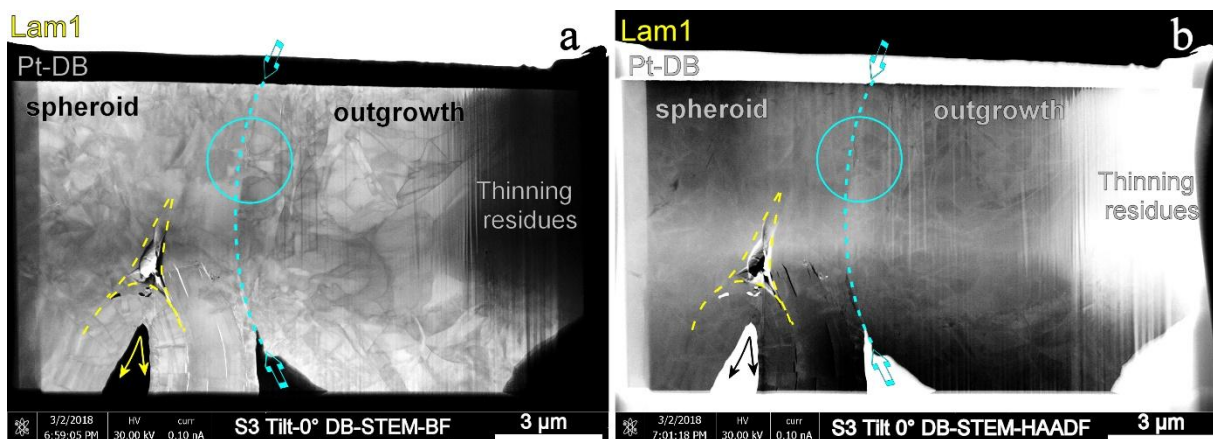


Fig. 6 DB-STEM-BF (a) and -HAADF (b) images of a thin lamella (Lam1) prepared through the outgrowth in figure 1 (its preparation was illustrated with Figs. 1 and 2). Note reverse contrast between BF and HAADF

images: dark (BF) versus bright (HAADF) bulk matrix, dark grey (BF) versus light grey (HAADF) grain boundaries, bright (BF) versus dark (HAADF) lack of matter (enclosed with a yellow curved triangle). The blue open arrows and blue dotted line mark the boundary between graphite layers associated to the spheroid and those to the outgrowth; hairpin curving of the graphite layers is indicated with solid arrows. The blue circle indicates the location of the nano-aggregates evidenced with the TEM-STEM observations presented in section 3.3.

It should first be noted that the protrusion appears as a plate extending below the original metallographic section, although it is not known whether its thickness (about 5 μm in Figure 1) was constant. In addition, it can be seen that a "leg" has developed between the spheroid and the outgrowth, to the right under the yellow dashed curved triangle. This leg is clearly associated with the spheroid above the hairpin curve marked with the two solid arrows in the micrographs. Based on the DB images, the graphite that grew on the spheroid and the graphite associated with the outgrowth can be distinguished, and the location of the interface between them is represented by a blue dotted line in the micrographs in figure 6. At this level of resolution, one can only observe that this interface exhibits a contrast differing from that of sub-grain boundaries in the spheroid and the outgrowth.

At this stage, a tentative schematic can be proposed for explaining the above observations. The triangle in Figure 6 represents a graphite-free area, without any matter, that may have been created due to competition between the two growing outer layers, one coming from the top and the other from the bottom in the image. The former forced the latter to adopt a hairpin growth pattern. Then, the continuous precipitation of graphite led to the merging of these ascending and descending layers giving what is called the leg. According to this schematic, the leg itself constitutes a protrusion, in which the graphite stacking is parallel to that of the underlying spheroid. On the contrary, the plate-like shape of the main protrusion suggests that its graphite stacking is perpendicular to that of the part of the spheroid which is seen in the micrographs. The latter finding suggests that the origin of the main protrusion could be outside the observable area.

In figure 7, the STEM images of the protrusion described in figure 5 suggest the lamella is slightly thicker than the previous lamella. Contrary to the previous case, the boundary between the spheroid and the protrusion could easily be located and is shown with a blue

dotted line in figure 7(a). However, higher magnification image in

Fig. 7(b) emphasizes the various orientations of the different crystallized domains. An intermediate region between the spheroid and the outgrowth is thus evidenced which has been delimited with blue dotted lines.

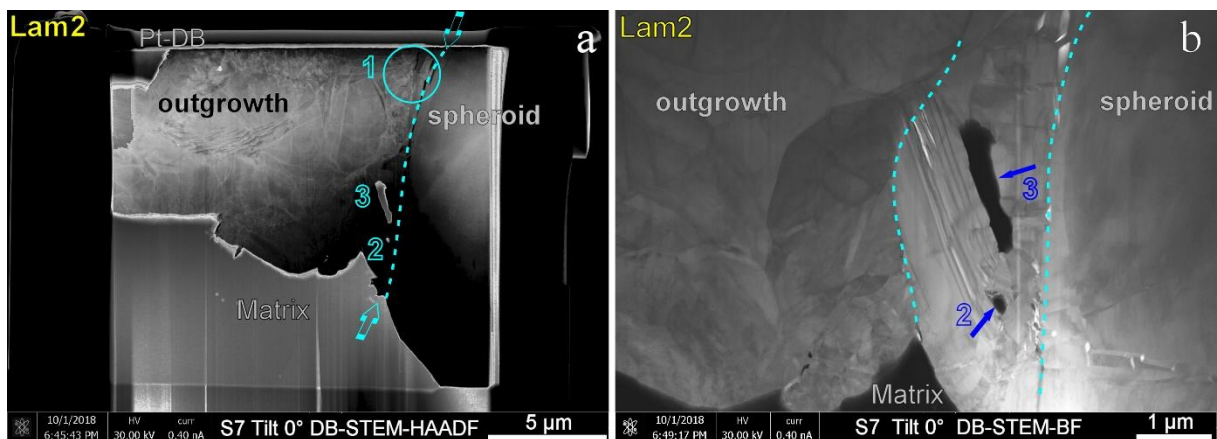


Fig. 7 (a) Low magnification DB-STEM-HAADF image of the thin lamella (Lam2) prepared through the outgrowth of figure 5. Dotted lines mark boundaries between the spheroid and the outgrowth (empty arrows). (b) Medium magnification DB-STEM-BF image showing an intermediate region between spheroid and outgrowth. The blue circle numbered 1 in (a) indicates the location of the nano-aggregates evidenced with the ARM observations presented in section 3.3. The areas numbered 2 and 3 are Fe-rich.

Some EDS analyses were carried out at different points of the lamella and are numbered on the images. They showed that the dark areas within the intermediate region (points 2 and 3) are iron-rich, with a composition close to that of the matrix. Here again, a schematic can be proposed that at first appears simpler than in the previous case: precipitation of graphite proceeded at the expense of the iron-rich matrix, which was thus present in all the space left by graphite. When the protrusion started to develop away from the spheroid, a space appeared which was iron-rich. At a later stage, this space became enclosed by graphite leading to the transition zone with iron-rich areas in it. However, it must be determined whether the matrix was liquid or solid at this stage, as this would give an essential hint about the process of

graphite degeneracy. Owing to the large amount of graphite in this zone compared to the quantity of iron-rich areas, it may be postulated that the matrix was liquid.

During the above DB-STEM study, special attention was put on the boundaries between the spheroids and the outgrowths. Nevertheless, this is only the TEM-STEM study to follow that evidenced the presence of nanoaggregates in the zones circled in blue in figure 6 and 7.

3.3. TEM-STEM in the ARM

STEM-BF observations in the DB only allowed visualization of the boundary between spheroid and outgrowth. Similarly, traditional TEM images as those in figure 8 only show nice mosaic-like contrasts revealing the different grains and sub-grains in the spheroid and the outgrowth of figure 6. Neither Selected Area Diffraction Patterns nor observations at high magnification and high resolution allowed distinguishing any particular feature along the supposed interface between the spheroid and the outgrowth that would provide any clue to the growth mechanism of the outgrowth. On one hand, the smallest available selected area aperture for diffraction pattern is 150 nm in diameter and only graphite electron diffraction patterns were observed. On the other hand, the formation of TEM images is mainly dominated by three contrast mechanisms: contrast due to diffraction and thickness-mass at low magnification and phase contrast at high magnification and resolution.

HAADF-STEM imaging in the atomic resolution microscope (ARM) helps going further as it associates Z-contrast and atomic resolution imaging thanks to the fact that the contrast is primarily dependent on mass-variations from one atom column to the other under the small electron probe during scanning. Even at medium magnification, tiny domains exhibiting a very bright contrast were thus observed near the expected spheroid-outgrowth interface (Fig. 8 (b)). For further emphasizing the difference between standard TEM images and the HAADF-STEM image of the ARM, the dashed green circle surrounding the bright spot in figure 8(b) has been located after proper sizing on the other three images. A careful comparison of images (b – HAADF-STEM) and (c – TEM) evidences that of the several dark areas in (c), only one appears to be very bright in (b). This means that all dark contrast areas in (c – TEM), but the one that is arrowed, are only related to diffraction mechanism. Finally, and for further illustration purpose, the area which is squared in figure 8(b) has been superimposed onto the TEM image after contrast reversal (Fig. 8 (d)).

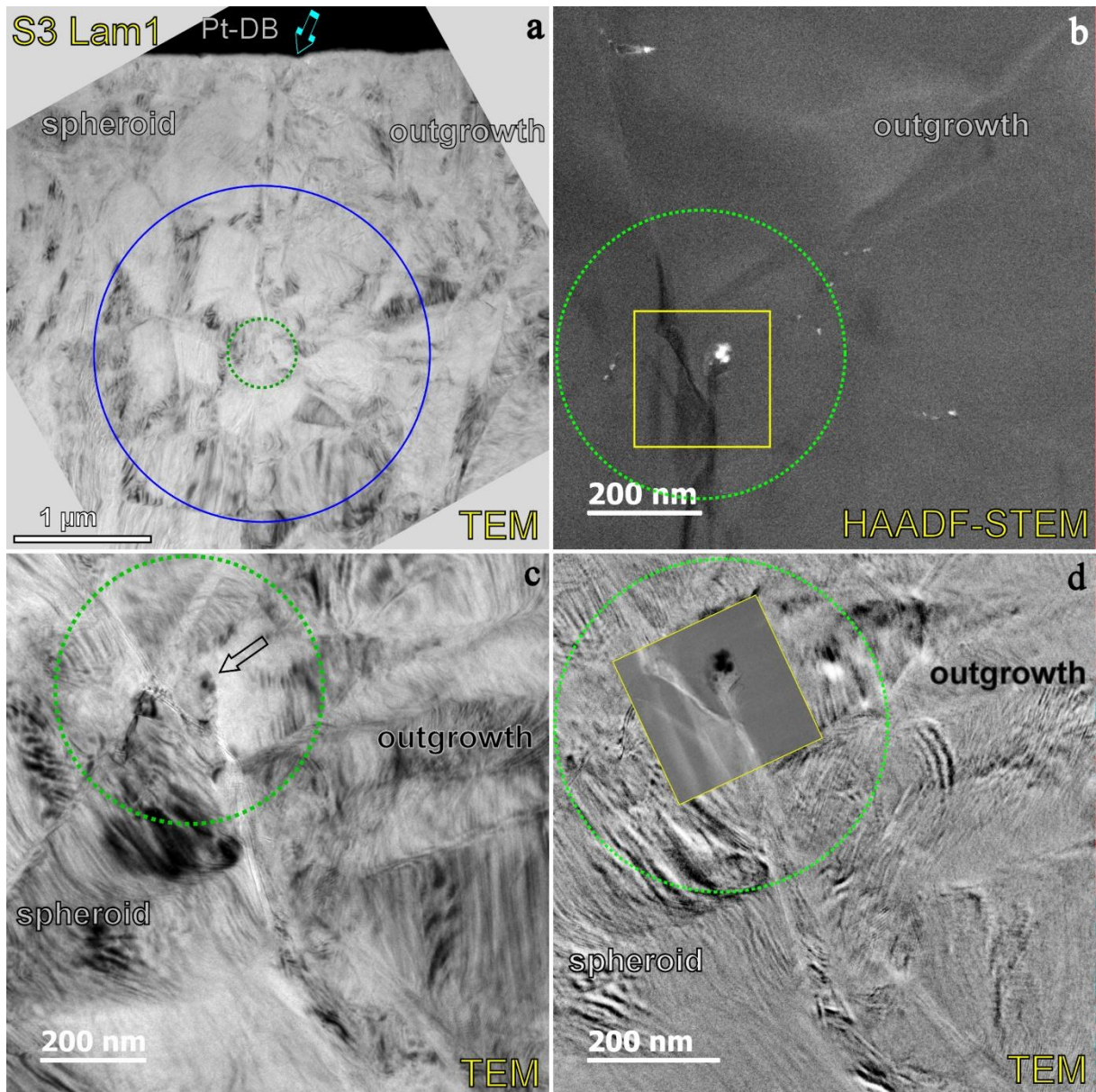


Fig. 8 TEM images at different magnifications (a, c and d) and related HAADF-STEM image (b) showing an inclusion exhibiting a bright contrast. This inclusion is arrowed in (c). The large blue circle in (a) corresponds to that drawn in figure 6; the dashed green circles in (a)-(d) mark out the same sample area; the squared area in the HAADF-STEM image (b) is superimposed in (d) after contrast reversal and appropriate tilting.

Similar observations were made on the second lamella (Fig. 9). To ease tracking of the area of interest on the lamella, the large solid circle in the TEM image of (a) corresponds to the circle in figure 7(a). Observation with HAADF-STEM detector allowed picking out tiny domains exhibiting a very bright contrast close to the spheroid-outgrowth interface. One such domain is arrowed in figure 9(b). The bright contrast of this inclusion in HAADF-STEM image (b) reverses to dark contrast in the BF-STEM image (c).



Fig. 9 TEM image (a), HAADF-STEM (b) and BF-STEM (c) images. The large solid circle corresponds to that in figure 7(a); dashed circles mark out the same sample area in the three images; the small arrows point to the small inclusion exhibiting a bright contrast on HAADF-STEM image (b) and a dark one on BF-STEM image (c).

The very bright contrast in the HAADF-STEM images in figures 8 and 9 suggests the presence of some heavy element(s). To confirm this, several EDS analyses were carried out on bright contrast areas and some neighboring areas for comparison. These areas are numbered on the four images in figure 10 which relate to lamella 1 (Lam1) and lamella 2 (Lam2). Table 2 gives the amount (at%) of elements that were detected (wt% can be found in the supplementary File). Ga appears that is due to milling process while Ce was never detected and thus was not listed in Table 2. In addition to the elements detected by EDS in the SEM, Ag, Pb and Sn were detected here. Thus, the heavy elements related to the present study are Pb which was effectively added and Ag and Sn which must have been present at low level in the metallic charge used to prepare the cast iron.

To emphasize trace elements, namely O, Mg, Al, S, Si, P, Ag, Sn and Pb, EDS measurements were normalized with the sum of their atomic contents ($O + Mg + Al + S + Si + P + Ag + Sn + Pb$). The resulting ratios (at %) are listed in Table 3. In this table, the results for areas #2 and #3 that mostly contain carbon with traces of oxygen are not reported. It was also noted that areas #11 and #12 contain mostly iron and could thus correspond to trapped matrix. This was confirmed with the HRTEM images of the latter areas that show crystallized

domains with planes spaced by 0.2 nm which can be indexed as d_{011} Fe-framework (

Fig. 11) and SAED patterns as well (see Suppl-Fig4). Accordingly, the results for areas #11 and #12 are not reported either in Table 3.

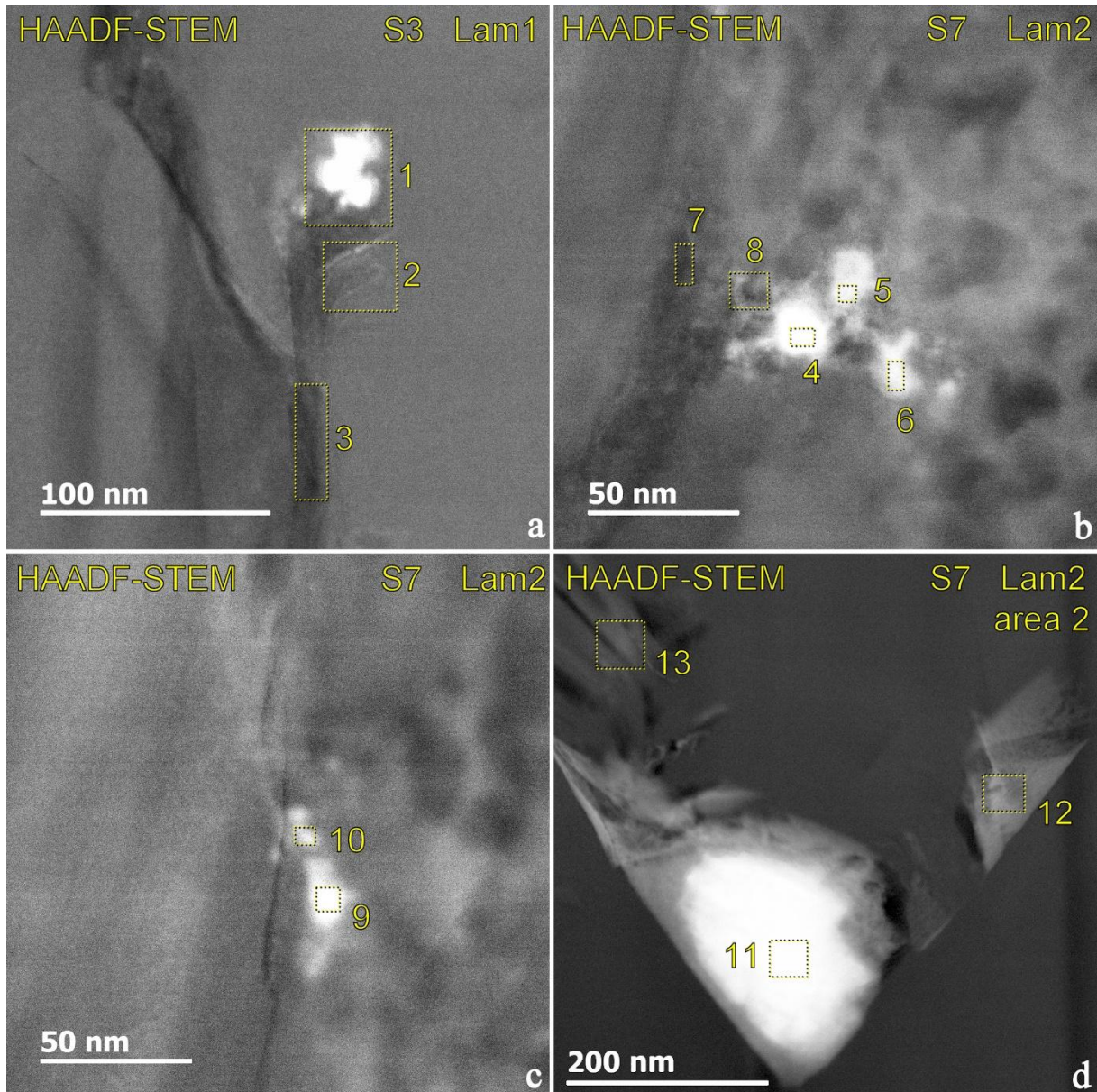


Fig. 10 HAADF-STEM images of lamella 1 (a) and lamella 2 (b-d) showing the areas selected for EDS analyses. Lam1 image corresponds to the yellow squared area in the STEM-DF image of figure8(b).

Several remarks can be drawn from EDS results shown in Table 3. Sn and Pb accumulated in several locations, either together (#1, #4, #5, #6, #8, #9 and #10) or separately (#7). Apart for location #13, Mg is always present at about the same level between 12 and 20 at% (10 and 20 wt%) and associated to the presence of Pb and/or Sn. It should be stressed that the Mg content is so much lower than the O content that these analyses could not correspond to MgO. The same stands for location #13 where only O and P were detected, with the former at a much higher level than the latter. The presence of oxygen must therefore be due to pollution during sample handling. Al was detected only in location #4 and at a fairly low level, it will not be examined further. Finally, since Mg, Pb and Sn do not form compounds at the temperature at which graphite grew during solidification of cast iron, they must have been

present in an elemental form during this transformation. In summary, it is very likely that the presence of Mg, Sn and Pb indicates that these elements were in an elemental form on the surface of the graphite nodule where they were trapped when the protrusion developed. The nanoscale precipitates would appear during cooling of the metal by diffusion of these elements at the interface between graphite and protrusions.

Table 2. EDS measurements (at.%) at the locations specified in figure 10.

Area	C	O	Mg	Al	Si	P	S	Fe	Ga	Ag	Sn	Pb
#1	93.6	3.0	0.5	*	*	*	*	*	0.2	*	0.3	0.1
#2	96.9	0.6	*	*	*	*	*	*	0.1	*	*	*
#3	96.6	1.0	0.1	*	*	*	*	*	*	*	*	*
#4	85.3	9.1	1.8	0.2	*	0.1	*	0.1	*	*	0.9	0.6
#5	90.9	5.5	1.4	*	*	*	*	0.1	0.1	*	0.5	0.1
#6	95.0	2.9	0.8	*	*	*	*	*	*	0.2	0.3	0.02
#7	94.0	4.4	0.7	*	*	*	0.3	*	*	*	*	0.1
#8	91.2	5.9	1.3	*	0.4	*	0.4	0.1	*	*	0.1	0.1
#9	94.4	3.0	0.7	*	*	*	*	*	*	*	0.4	0.1
#10	95.0	3.2	0.9	*	*	*	*	*	*	0.1	0.1	0.1
#11	21.7	12.4	0.8	1.0	3.3	0.8	*	50.2	0.2	0.1	*	0.1
#12	77.8	16.4	0.9	*	0.6	0.3	*	2.8	0.1	0.02	*	*
#13	97.3	1.6	*	*	*	0.2	*	0.1	*	*	*	*

* means that element either was not detected or its quantification result was $< 2\sigma$.

Table 3. Normalized (at%) EDS measurements on trace elements (see text) at the locations specified in figure 10.

Area	O	Mg	Al	Si	P	S	Ag	Sn	Pb
#1	76.9	12.8	*	*	*	*	*	7.7	2.6
#4	71.7	14.2	1.6	*	0.8	*	*	7.1	4.7
#5	73.3	18.7	*	*	*	*	*	6.7	1.3
#6	69.0	19.0	*	*	*	*	4.8	7.1	0.5
#7	80.0	12.7	*	*	*	5.5	*	*	1.8
#8	72.0	15.9	*	4.9	*	4.9	*	1.2	1.2
#9	71.4	16.7	*	*	*	*	*	9.5	2.4
#10	72.7	20.5	*	*	*	*	2.3	2.3	2.3
#13	88.9	*	*	*	11.1	*	*	*	*

* means that element either was not detected or its quantification result was $< 2\sigma$.

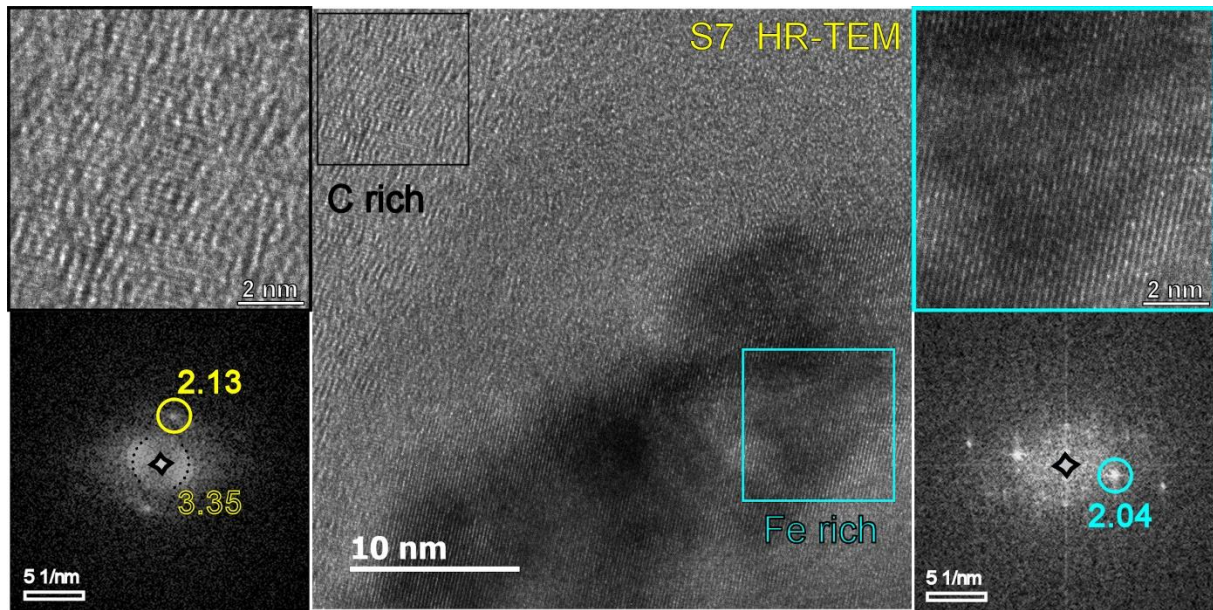


Fig. 11 HR-TEM image taken on the border of a Fe-rich area (Lam2); the two inserts on the left side are an enlargement of the squared C-rich area and its FFT-transform, showing this corresponds to graphite; the two inserts on the right side are an enlargement of the blue squared Fe-rich area and its FFT-transform corresponding to Fe-rich ferrite, inter-reticular distances appearing in the FFT images are given in Å.

3.4. ACOM Results

The study of graphite orientation in the lamella 2 (

Fig. 7) was performed by ACOM measurements. Figure 12 (a) shows the DB-STEM-BF image of the region analyzed with ACOM. The orientation map corresponding to this region is presented in Figure 12(b). In the latter image, both black long dashed lines delineate the outer layer of the spheroid but also define a transition zone between the nodule to the left and the plate-like outgrowth to the right. The arrow labelled r represents the radial direction in the nodule.

On the DB-STEM-BF image of figure 12a, it is seen that the contrast within the nodule and within the bottom part of the protrusion is even, while an area showing different contrasts is seen in the middle of the image at the right of the transition zone. Within this area, the dark elongated zone is a trapped matrix Fe-rich domain. The ACOM map confirms that graphite around this particle shows various orientations in agreement with previous work [33] where this phenomenon was associated to the disturbance of graphite growth generated by iron inclusions (see an example in HR-TEM image of Suppl-fig5). For clarity, matrix areas appear in white on ACOM map.

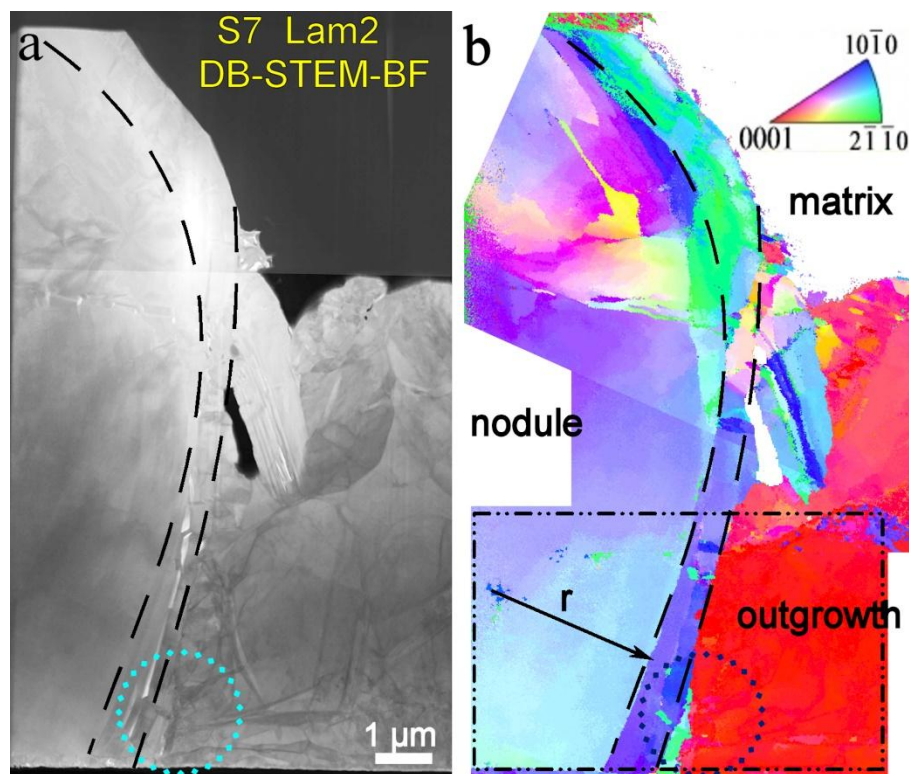


Fig. 12 (a) DB-STEM-BF image of the interface region between the nodule and outgrowth in the lamella 2; (b) corresponding crystal orientation map, excepted matrix areas in white, with the reference triangle; the blue dotted circles are the same as the one in figure 7(a) with its center corresponding to the location of the nano-aggregates.

Focus was then put on the lower part of the investigated area within the dash-dot box for a detailed analysis of misorientation within and between the three zones, namely the nodule, the transition zone and the protrusion. Within the nodule, measurements of misorientation along lines perpendicular and parallel to the radial direction were carried out and showed values of 12° at the most, regardless of the direction of the measurements. With a maximum at 4° , the misorientation spread in the outgrowth was found to be far lower.

Several misorientation line analyses were then recorded starting in the nodule and ending in the outgrowth as the one illustrated in figure 13. The results indicate that there is an

overall righting of the c axis of graphite of ($\sim 76^\circ$) between the nodule and the outgrowth, with an intermediate rotation corresponding to the transition zone. The orientation change between the nodule and the transition zone corresponds to a simple rotation of about 16° around an axis close to c axis, situated in (a, c) plane, as schematically represented with the projection views of the hexagonal cell. From the transition zone to the green region, there is an additional rotation of about 26° around another axis close to c axis, but situated in $(a-b, c)$ plane. The final rotation between the green region and the outgrowth is of about 86° around an axis close to a , situated in the (a, c) plane. Each misorientation jump from one region to another is indicated by an arrow in the diagram point to point of Figure 13.

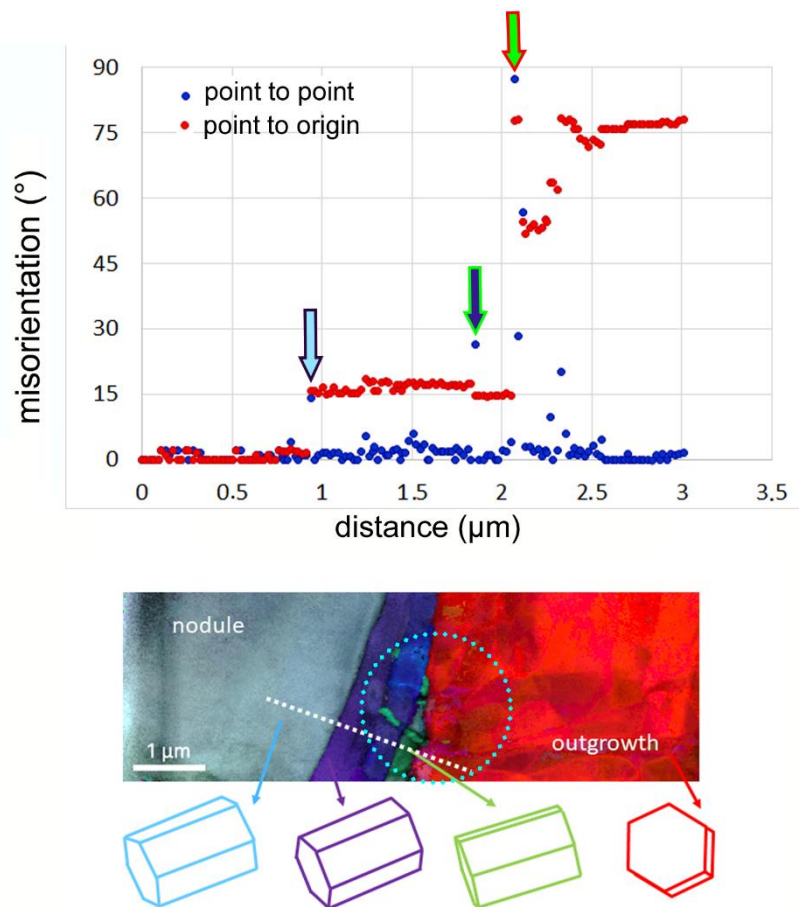


Fig. 13 Misorientation profiles between the nodule and the outgrowth measured along the white dotted line in the IPF map; red dots give the misorientation with respect to the origin of the X axis, blue dots give the misorientation from one to the next point along the dotted line; arrows point out the misorientation gap from nodule to transition, then to green zone and finally to outgrowth; projection views of the hexagonal cell have been added to ease visualizing the changes in orientation; nano-aggregates are localized at the center of the blue dashed circle.

4. Discussion

Magnesium is the most effective element known for spheroidizing graphite in cast irons, though it is sometimes complemented with rare earths which enhance melt deoxidization and desulphurization. The effectiveness of magnesium is however countered by many other elements such as Pb and Sn that were studied in the present work. Recently, ab initio calculations showed that most of the elements of the Mendeleev table are prone to adsorb on the prism planes of graphite where carbon atoms do also add up for graphite crystallization [19]. This supports a schematic in which magnesium spheroidizes graphite by decreasing the rate of growth of graphite along the prism planes. An interesting output from these ab initio calculations was that magnesium is the element showing the lowest adsorption energy amongst the many elements for which calculations were performed. This means that any impurity is adsorbed preferentially to magnesium, thus hindering the role of this latter. In the following, the results of the present investigation are discussed to see if they support the above schematic. More precisely, the discussion follows two lines: i) adsorption and absorption of magnesium; ii) relation between impurity elements and formation of protrusions.

4.1. Absorption of magnesium in graphite

Complementing chemical analyses mentioned in the introduction, TEM observations have already demonstrated that foreign elements may be incorporated in graphite [34-35, 27]. All authors of these observations suggested that foreign elements get intercalated between graphite layers instead of being substituted to carbon atoms. Purdy and Audier [34] and Miao et al. [35] were looking at cerium and assumed it was present in graphite as oxide, while Qing et al. [27] claimed that the several foreign elements (Mg, Ce, La) they measured were present in their elemental form. The latter authors observed also by atom probe tomography that nickel, calcium, aluminum and phosphorus showed a higher content in graphite than in the surrounding matrix which was liquid at the time graphite precipitated. Unfortunately, they could not measure magnesium because of mass interferences with carbon.

Focusing on magnesium, it is considered that it enters graphite during solidification of cast iron melts having received a spheroidizing treatment with this element. However, such intercalated elements disturb the graphite stacking and may be rejected afterwards. For example, during slow cooling or if the casting is heat-treated after complete solidification, magnesium may then be expelled out from bulk graphite and accumulate at the

graphite/matrix interface as previously observed [26, 18]. The present results evidenced magnesium accumulation at the outer surface of graphite, in agreement with the slow cooling of the investigated material [28]. They also show that magnesium is most often associated with Sn and Pb.

This competition between absorption during graphite growth and rejection for increasing graphite crystallinity may explain some of the contradictory reports found in the literature. Considering that magnesium enters in graphite during growth from the liquid means that the remaining liquid becomes impoverished in magnesium during primary graphite precipitation. However, the solubility of magnesium in austenite is lower than in liquid which leads to an overall increase in the magnesium content in the liquid once eutectic solidification has started. This schematic might explain several experimental observations on the change in shape of graphite during solidification of cast irons. The most obvious of these observations is solidification of so-called compact graphite cast irons in which graphite first precipitates as spheroids from the liquid, then develops in two-phase graphite-austenite eutectic cells where graphite has a coarse lamellar shape, and finally may again assume a spheroidal shape in the last to freeze areas [36 – 37]. These three steps may be straightforwardly related to impoverishment and then enrichment in magnesium of the remaining liquid.

4.2. Relation between impurity elements and formation of protrusion

It is the first time that TEM is used to evidence the presence of foreign elements at the interface between a nodule and a protrusion as seen in figure 10. It may be thought that the observed accumulation of Pb and Sn was instrumental to the development of the protrusion by perturbing the normal spheroidal growth process triggered by magnesium. The plate-like shape of all the protrusions which have been observed in this work suggested they grew along the prismatic direction of graphite as does lamellar graphite and this has been verified with ASTAR (figure 12). The protrusions may have formed according to one of the two following processes:

- As a coupled growth of austenite and graphite. Instead of being fully encapsulated by austenite, graphite spheroids develop outgrowth which then grow as a coupled eutectic, i.e. with both phases in contact with the liquid. This seems to be the case in the observation of quenched samples by Stefanescu et al. [8] where graphite spikes protruding out from spheroids were found to be in contact with cementite plates formed from the surrounding liquid during quenching. It has been recently reported that plate-like and lacy forms of graphite appearing in the last to freeze areas of a

spheroidal graphite cast iron are indeed connected to the spheroids [28]. Such a continuity may share some common characteristics with compacted graphite [38 – 40] and thus demonstrate coupled growth.

- In solid state, once the graphite has been encapsulated by austenite during the eutectic reaction or later during cooling after complete solidification. That this may happen after complete solidification is demonstrated by the possibility of solid-state graphitization of cast irons solidified partly or fully in the metastable system, see for example the recent work by Bourdie [41]. As for solidification, there is no definite proof though Bjerre could describe his synchrotron in-situ observations by this mechanism [42].

The present results do not allow deciding which of the above processes was involved in the present study but give some new views about the evolution of the graphite packing at the outer surface of the spheroids and in the protrusions. Figure 3 illustrates that at the base of a protrusion the graphite stacking shows several direction changes at a scale of a few micrometers. Previous studies on branching in lamellar graphite [16, 17] and on initial growth of spheroidal graphite [27] demonstrated the close relation of such perturbations with intercalation of foreign elements within graphite. The outgrowth in figure 3 seems to have started in the zone between two sub-sectors which is intrinsically a zone where graphite stacking is perturbed [43]. As a consequence, the growth direction of the protrusions may have little to do with the crystallographic orientation of graphite in the spheroid at the base of the outgrowth as effectively observed in the present work.

5. Conclusion

Several advanced electron microscopy tools have been used to bring to light the presence of trace elements including magnesium in relation to the development of protrusions onto spheroidal graphite. EDS measurements on graphite protrusions in FIB-prepared thin foils suggest that magnesium and phosphorus are present at the outer surface of graphite, i.e. at the interface between graphite and the surrounding matrix. HR-TEM-STEM allowed going further by evidencing the presence of heavy elements (Ag, Pb and Sn) at the interface between spheroids and protrusions developing from them. This supports a schematic in which such impurities when present adsorb preferentially to magnesium onto the prismatic planes of graphite, thus perturbing spheroidal growth. Finally, ACOM showed that there is no special crystallographic relationship between plate-like protrusions and underlying spheroid.

Acknowledgments

This work was performed with the financial support of the program EQUIPEX GENESIS, Agence Nationale de la Recherche (ANR-11-EQPX-0020) for studies in the Dual Beam system.

References

- [1] H. Morrogh, W.J. Williams, The production of nodular graphite structures in cast iron, *JISI* 156 (1948) 306-322.
- [2] K.D. Millis, A. P. Gagnebin, N. B. Pilling, Cast ferrous alloy, patent 2,485,760.
- [3] B. Lux, On the theory of nodular graphite formation in cast iron- Part I: experimental observations of nodular graphite formation during the solidification of cast iron melts, *AFS Cast Metals Res. J.* 3 (1972) 25-38.
- [4] J. Lacaze, L. Magnusson-Åberg, J. Sertucha, Review of microstructural features of chunky graphite in ductile cast irons, *Proc. Keith Millis symposium*, AFS, 2013, 232-240.
- [5] W. Baer, Chunky graphite in ferritic spheroidal graphite cast iron: formation, prevention, characterization, impact and properties – an overview, *Int. J. MetalCast.*, 2019, <https://doi.org/10.1007/s40962-019-00363-8>.
- [6] T. Thielemann, Zur Wirkung von Spurenelementen im GuBeisen mit Kugelgraphit, *Giessereitechnik* 16 (1970) 16-24.
- [7] A. Reynaud, *Oligo-éléments et fontes*, éditions ETIF, 2005.
- [8] D.M. Stefanescu, G. Alonso, P. Larranaga, R. Suarez, On the stable eutectic solidification of iron-carbon-silicon alloys, *Acta Mater.* 103 (2016) 103-114. DOI: 0.1016/j.actamat.2016.01.047.
- [9] J. Lacaze, J. Bourdie, M.J. Castro Roman, A 2-D nucleation-growth model of spheroidal graphite, *Acta mater.* 134 (2017) 230-235. DOI : 10.1016/j.actamat.2017.05.032;
- [10] J.E. Rehder, Nodules and nuclei in nodular iron, *Amer. Foundrym.* 21 (1952) 44-48 and 87-90.
- [11] A. Wittmoser, Sur les germes du graphite spheroidal, *Fonderie* (1954) 4128-4145.
- [12] B. Francis, Heterogeneous nuclei and graphite chemistry in flake and nodular cast iron, *Metall. Trans. A.* 10A (1979) 21-31.

- [13] S.E. Franklin, R.A. Stark, Application of secondary ion mass spectrometry to study of graphite morphology in cast iron, *Metal Science* 18 (1984) 187-200.
- [14] S.E. Franklin, R.A. Stark, Further use of secondary ion mass spectrometry in the study of graphite morphology control in cast irons, *MRS Symp. Proc.* 34 (1985) 25-35.
- [15] G. Torga, R. Boeri, F. Weinberg, Trace elements in nodular and compacted graphite in cast iron, *Cast Metals* 2 (1989) 169-174.
- [16] N. Valle, K. Theuwissen, J. Sertucha, J. Lacaze, Effect of various dopant elements on primary graphite growth, *Proc. Conf. ICASP-3, IOP Conf. Ser.: Mater. Sci. Eng.* 27 (2011) 012026. DOI: 10.1088/1757-899X/27/1/012026.
- [17] J. Lacaze, N. Valle, K. Theuwissen, J. Sertucha, B. El Adib, L. Laffont, Redistribution and effect of various elements on the morphology of primary graphite growth in cast iron, *Advances in Materials Science and Engineering*, 2013, ID 638451. DOI: 10.1155/2013/638451.
- [18] J. Bourdie, F. Bruneseaux, P. de Parseval, S. Gouy, L. Laffont, J. Lacaze, Effect of cooling rate and aluminium addition on graphite growth and graphitization of thin wall castings, *Proc. Conf. Science and Processing of Cast Iron, SPCI-XI, Materials Science Forum*, 925, 2018, 20-27. DOI: 10.4028/www.scientific.net/MSF.925.20.
- [19] J. Lacaze, D. Connétable, M.J. Castro de Roman, Effects of impurities on graphite shape during solidification of spheroidal graphite cast irons, *Materialia* 8 (2019) 100471. DOI: 10.1016/j.mtla.2019.100471.
- [20] J.S. Park, J.D. Verhoeven, Transitions between type A flake, type D flake, and coral graphite eutectic structures in cast irons, *Metall. Mater. Trans.* 27A (1996) 2740-2753.
- [21] J.D. Verhoeven, A.J. Bevolo, J.S. Park, Effect of Te on morphological transitions in Fe-C-Si alloys: Part II. Auger analysis, *Metall. Trans.* 20A (1989) 1875-1881.
- [22] B.C. Liu, T.X. Li, Z.J. Rue, X.Y. Yang, E.Q. Huo, C.R. Loper, The role of antimony in heavy-section ductile iron, *AFS Trans.* (1990) 753-757.
- [23] L. Dekker, B. Tonn, G. Lilienkamp, Effect of antimony on graphite growth in ductile iron, *Int. J. Metalcasting*, DOI: 10.1007/s40962-020-00434-1.
- [24] J.C. Sawyer, J.F. Wallace, Effects and neutralization of trace elements in gray and ductile irons, *Trans. AFS* 76 (1968) 386-404.
- [25] H. Itofuji, H. Uchikawa, Formation mechanism of chunky graphite in heavy-section ductile cast irons, *AFS Trans.* 98 (1990) 429-448.

- [26] P. Dierickx, C. Verdu, A. Reynaud, R. Fougères, A study of physico-chemical mechanisms responsible for damage of heat-treated and as-cast ferritic spheroidal graphite cast irons, *Scr. Mater.* 34 (1996) 261-268.
- [27] J. Qing, M. Xu, V. Pikhovich, Why is Graphite Spherical in Ductile Iron? A Study of Elements in the Spheroidal Graphite Using Atom Probe Tomography and Transmission Electron Microscopy, *Proc. Keith Millis symposium, DIS*, 2018.
- [28] B. Tonn, J. Lacaze, S. Duwe, Degenerated graphite growth in ductile iron, *Proc. Conf. Science and Processing of Cast Iron, SPCI-XI, Materials Science Forum*, 925 (2018) 62-69. DOI: 10.4028/www.scientific.net/MSF.925.62.
- [29] T. Yaguchi, T. Kamino, T. Ishitani, R. Urao, Method for Cross-sectional Transmission Electron Microscopy Specimen Preparation of Composite Materials Using a Dedicated Focused Ion Beam System, *Microsc. and Microanal.*, 5(5) (1999) 365–370.
- [30] LA. Giannuzzi, F.A. Stevie, editors. *Introduction to focused ion Beams. Instrumentation, Theory, techniques and Practice*. New York: Springer (2005).
- [31] NanoMEGAS website: <http://nanomegas.com>.
- [32] E.F. Rauch, M. Véron, Automated crystal orientation and phase mapping in TEM, *Materials Characterization* 98 (2004) 1-9. DOI: 10.1016/j.matchar.2014.08.010.
- [33] K. Theuwissen, J. Lacaze, M. Véron, L. Laffont, “Nano-scale orientation mapping of graphite in cast irons”, *Mater. Charac.* 95 (2014) 187-191. DOI: 10.1016/j.matchar.2014.06.021.
- [34] G.R. Purdy, M. Audier, in *The Physical Metallurgy of Cast Irons*, (eds) Fredriksson H, and Hillert M, North-Holland, Elsevier Science Publishing Co. Inc., Amsterdam, *MRS symposia proceedings* 34 (1985) 13.
- [35] B. Miao, D.O. Northwood, W. Bian, K. Fang, M.F. Fan, Structure and growth of platelets in graphite spherulites in cast irons, *J. Mater. Sci.* 29 (1994) 255-261.
- [36] M. König, *Microstructure Formation During Solidification and Solid State Transformation in Compacted Graphite Iron*, Chalmers University of Technology, Sweden, 2011.
- [37] M. Gorny, Cast iron: compacted graphite, *Encyclopedia of Iron, Steel, and Their Alloys*, Taylor & Francis, 2015, 718-734. DOI: 10.1081/E-EISA-120050773.
- [38] Den Xijun, Zhu Peiyue, Liu Qifu, Structure and formation of vermicular graphite, *Mat. Res. Soc. Symp. Proc.* 34 (1985) 141-150.
- [39] G.X. Sun, Study on the morphology and growth pattern of C/V graphite, *Conf. Proc. of Cast Iron IV, MRS*, 1990, 57-64.

- [40] C. Chuang, D. Singh, P. Kenesei, J. Almer, J. Hryn, R. Huff, 3D quantitative analysis of graphite morphology in high strength cast iron by high-energy X-ray tomography, *Scr. Mater.* 106 (2015) 5-8; and <https://www.anl.gov/article/highenergy-xrays-give-industry-affordable-way-to-optimize-cast-iron>.
- [41] J. Bourdie, Sphéroïdisation du graphite - Cas de la fonte centrifugée, PhD thesis, Université de Toulouse, INPT, 2017. <https://oatao.univ-toulouse.fr/19739/>.
- [42] M. K. Bjerre, In situ observations of graphite formation during solidification of cast iron, PhD Thesis, DTU, Lyngby, Denmark, 2017. <https://orbit.dtu.dk/en/publications/in-situ-observations-of-graphite-formation-during-solidification->.
- [43] K. Theuwissen, J. Lacaze, L. Laffont, Structure of graphite precipitates in cast iron, *Carbon* 96 (2016) 1120-1128. DOI: 10.1016/j.carbon.2015.10.066.